Supporting Information for

Structural fluctuations cause spin-split states in tetragonal $(CH_3NH_3)PbI_3$ as evidenced by the circular photogalvanic effect

Niesner et al. 10.1073/pnas.1805422115

1. Experimental details

A. Fabrication and characterization of $(CH_3NH_3)PbI_3$ single crystal devices. $(CH_3NH_3)PbI_3$ single crystals were grown by the bottom seed solution growth method as reported in literature (1). Details of the crystal growth and characterization are given in Ref. (2) and its supplementary online materials. Crystals were transferred through air and 70 nm of gold were thermally evaporated on the crystals with a spacing of 1 mm to form the contacts. The contacts were aligned with the macroscopic edges of the crystals. Crystals were stored under nitrogen atmosphere for several days and no longer than four weeks prior to the photocurrent measurements.

B. Setup for photocurrent measurements. Photocurrents are excited with a Ti:Sa laser. The excitation laser power ranged from 5 μW to 3 mW (exceeding 40 μW only when the sample was cooled to 4 K). Experiments were done both with the laser in cw and pulsed (15 kHz repetition rate, 100 fs pulse duration) mode giving similar results. The laser beam was chopped at a rate of 1180 Hz, and the photocurrent is measured using a lock-in amplifier.

Two different cryostats were used for the experiments, one containing a helium-cooled coldfinger and a fine translational stage for spatially resolved measurements at low temperature. The other one is a He flow cryostat for angle-dependent measurements. For measurements at room temperature, the sample was kept in a nitrogen atmosphere. For temperature-dependent and low-temperature experiments, the sample was in vacuum.

Because of the well-known possible sample-to-sample variations and limited stability of $(CH_3NH_3)PbI_3$ we performed measurements on a total of eight devices, see also table S1. The reported CPE was measured on all samples, even though the amplitude of the excited photocurrents varied from device to device and with the time after the first measurements. Generally, the photocurrent increases as the samples age and the CPE amplitude is reduced. Because of this sample degradation, data reported here were recorded on different devices, within 48 h after mounting them in the cryostat for measurements and starting the illumination.

C. Analysis of polarization-dependent photocurrent measurements. To measure the dependence of the photocurrent on the light polarization, a $\lambda/4$ waveplate is introduced in the excitation beam. Photocurrents are recorded continuously while the waveplate is rotated at low speed (36 s/turn). The resulting raw data are shown in figure S1 (a). They show a polarization-independent current of several nA, most probably due to a photo Dember effect and a photovoltaic effect caused by a band bending at the electrodes. To extract the photogalvanic effect, slow fluctuations in the photocurrent, which are caused by fluctuations in the laser power and changes in the sample at room temperature, need to be subtracted. We therefore average the photocurrent within an interval $[\alpha - 180°, \alpha + 180°[$ around each waveplate angle α and subtract this average. The extracted polarization-dependent photocurrents are given in figure S1 (b). This photocurrent is then back-folded into the interval $[0, 360°[$, see figure S1 (c). Finally, data points are averaged with a step width of 1°, figure S1 (d).

D. Measurements of the photoconductivity. For photoconductivity measurements, the voltage applied to the sample was swept under the same illumination conditions that were used for polarization-dependent measurements. The voltages applied did not exceed $V_{max} = 0.5$ V and the voltage was swept in a symmetrical way (0 V to V_{max}, V_{max} to $-V_{max}$, $-V_{max}$ to 0 V). We then extract the photoconductivity as the maximum slope of a linear fit to the $\Delta I/\Delta U$ during the V_{max}-to-$-V_{max}$, see figure S2. The resulting conductivity is given in Figure 3 of the main manuscript. Since the photoconductivity of lead halide perovskite devices can be substantially altered if a bias voltage was applied (3–5), all CPE measurements discussed in this work were recorded before the voltage sweeps were performed.

E. Photoluminescence spectroscopy and extraction of the direct optical band gap. In order to estimate the direct optical band gap of the $(CH_3NH_3)PbI_3$ perovskite single crystals under investigation, we employ photoluminescence spectroscopy. Photoluminescence was excited with a 532 nm cw laser between photocurrent measurements. Steady-state spectra were recorded using a OceanOptics QE spectrometer after suppressing the laser line with a dielectric 550 nm longpass filter. The resulting photoluminescence spectra are given in figure 5 of the main manuscript for different temperatures.

Figure S3 (a - d) shows a representative spectrum recorded at 270 K, as well as fits to the data based on different models. For direct semiconductors, the photoluminescence spectrum arising from purely electronic transitions (not involving the generation or annihilation of phonons) is given by the product of the absorption spectrum $A(E)$ and the Boltzmann distribution $f_B(E) = \exp(-E/kT)$, where E is the photon energy (6). We modelled the data using two different types of absorption spectra. The first one assumes only band-to-band transitions, without inclusion of excitonic effects. The resulting $A^{(a)}(E) = (E - E_{gap})^n \cdot \theta(E - E_{gap})$ reflects the joint density of states of the valence and conduction bands. Here, $\theta(E)$ denotes Heavyside's theta function. The photoluminescence intensity is then given by

$$I_{PL}^{(a)} \propto (E - E_{gap})^n \cdot \theta(E - E_{gap}) \cdot \exp(-E/kT) \qquad [1]$$

where E_{gap} denotes the transport gap (energy difference between conduction band minimum and valence band maximum). Equation 1 with $n = 1/2$ describes, for example, the photoluminescence spectrum of GaAs at room temperature very well. Larger n are possible if dipole transitions between the valence and conduction band edges are symmetry-forbidden. A fit of equation 1 to the data is shown in figure S3 (a). Even though we chose n to be a fit parameter, resulting in $n \approx 4$, the agreement between this model and the data is poor.

To refine the approach, we use an absorption spectrum derived from the Elliot model (7–9). This model takes into account both excitonic and band-to-band transitions, giving the absorption spectrum

$$A^{(b)}(E) = \frac{C_{b-b}}{E^2} \frac{1 + \mathrm{erf}\left(\left(E - E_{gap}\right)/\gamma\right)}{1 - \exp\left(-2\pi^2 \left|E_{x1}/\left(E - E_{gap}\right)\right|\right)} + \frac{C_{exc}}{E^2} \sum_{n=1}^{3} \left(\gamma n^3\right)^{-1} \exp\left(-\left(\frac{E - \left(E_{gap} - E_{x1}/n^2\right)}{\gamma}\right)^2\right) \quad [2]$$

where C_{b-b} and C_{exc} are the probabilities for band-to-band and excitonic recombination, E_{x1} is the binding energy of the first exciton (we use $E_{x1} = 16$ meV from Ref. (10)), and γ is a broadening parameter. A fit of $A^{(b)}(E) \cdot f_B(E)$ to the data is shown in figure S3 (b). The fitting curve matches the data well. We note that $C_{exc} \gg C_{b-b}$ in the fits, consistent with an assignment of the photoluminescence to recombination via excitonic transitions.

Alternatively, the broad photoluminescence spectrum of $(CH_3NH_3)PbI_3$ might arise from carrier-carrier recombination involving the creation or annihilation of phonons and molecular vibrations (11). In this case, each vibrational mode should generate a photoluminescence spectrum similar to the one described by equation 1 for $n = 1/2$, shifted by the vibrational energy to lower (phonon creation) or higher (phonon annihilation) energy with respect to E_{gap}. The width of the experimental spectrum (≈ 100 meV) is much larger than the one expected from equation 1 (≈ 40 meV for $n = 1/2$), suggesting that various vibrational modes which are not individually resolved contribute to the spectrum. This broadening could also be seen as the result of a disordered electronic potential energy landscape due to structural fluctuations. To model a broad distribution of unresolved, narrow photoluminescence peaks, we use a convolution of a Gaussian and a Boltzmann distribution, the latter reflecting the thermal broadening from equation 1. The resulting fitting curve is shown in figure S3 (c). The agreement between the data and this model is as good as with the model described by equation 2.

For reasons of completeness, we also determine the position of the maximum in the photoluminescence spectra by fitting a Voigtian function to the data as shown in figure S3 (d).

The band gaps estimated using the different approaches are summarized in figure S3 (e). With the exception of the modeling based on equation 1, which matches the data poorly, all models give similar temperature dependences. However, the absolute values of the extracted band gaps vary by tens of meV. In the main manuscript, we decide to give the results from the model using a Gaussian distribution of phonon-assisted emission peaks and a thermal population of electronic states. This interpretation of the photoluminescence spectra is in agreement with the literature implying strong electron-phonon coupling in perovskites (11–13), and the resulting band gaps are in line with the ones found from transmission measurements on thin films (14).

Thermal broadening is negligible for the modeling of the photoluminescence spectra recorded at 4 K in the orthorhombic phase, figure S4. This photoluminescence spectrum has a substructure, which we model by a sum of three Gaussian peaks. Using this approach, we find a high-energy emission feature at 1.64 ± 0.01 eV, a second peak at 1.61 ± 0.01 eV, and broad low-energy continuum emission with a maximum at 1.56 ± 0.01 eV, in agreement with previous reports (15–18). The positions of the maxima are indicated by tick marks. Following the literature (16, 19), we assign the highest-energy peak at 1.64 eV to the direct optical band gap of orthorhombic $(CH_3NH_3)PbI_3$.

2. Additional photocurrent measurements

A. Dependence of the CPE on experimental geometry. Figure S5 shows the polarization-dependent changes in the photocurrent for different geometries. When the beam fully illuminates the device (a), the CPE effect is roughly one order of magnitude stronger than in case of a focused beam (b). In the former case, electron-hole pairs are generated closer to the contacts, whereas in case of a focused (50 μm diameter) beam the carriers need to travel further before they are extracted. The increased number of scattering events results in a reduced influence of the optical transition that initially excites the photocurrent.

If the device is rotated by 90°, the CPE is reduced by at least two orders of magnitude and vanishes within the experimental uncertainties. This behavior is expected for a CPE resulting in a transverse photocurrent (see also figure 1 of the main manuscript) and has similarly been observed for the bulk Rashba system BiTeBr (20).

B. Spatially resolved photocurrent. To check the homogeneity of the $(CH_3NH_3)PbI_3$ single-crystal devices and estimate the size of the laser spot, current maps were recorded. The device is placed on two linear stages in the cryostat that allow positioning along both directions with a precision of ≈ 50 nm. A photocurrent map is given in figure S6 (a) for $(CH_3NH_3)PbI_3$ in the orthorhombic phase (4 K). We find a non-vanishing photocurrent for all positions of the laser spot, probably due to asymmetries in the gold contacts. Scanning the laser across the channel and the gold contacts along the y direction gives a mirror symmetric current profile, see figure S6 (b). The laser spot size was estimated from approximating the interfaces between $(CH_3NH_3)PbI_3$ and the gold contacts as a step function and convolving with a Gaussian reflecting the radius of the laser spot. We find a Gaussian spot diameter of 0.6 mm in this "moderately focused" geometry.

C. Linearity of the photocurrent. Figure S7 shows the photocurrent measured at a fixed photon energy (1.66 eV) and bias voltage (−0.25 V) as a function of excitation density. For a laser power < 1 mW the photocurrent increases linearly with excitation density.

3. Estimating the Rashba parameter from the experimental data

Within the Rashba model, the dispersion of the valence and conduction band is described by

$$E_i(k) = E_i(0) + (-1)^i \frac{\hbar^2 k^2}{2m_i^*} + (-1)^i \alpha_i k$$

with $i = 1$ for valence band and $i = 2$ for the conduction band. Here, $E_i(0)$ is the energy of the band of the band at the high-symmetry point, m_i^* is the carrier effective mass, and α_i is the Rashba parameter of the corresponding band. In reasonably good agreement with calculations (21, 22), we assume $m_1^* = m_2^* = m^*$. The transition energy between the bands is given by the energy difference $E_{21} = E_2(k) - E_1(k)$. The transition energy has its minimum for $\frac{\partial E_{21}}{\partial k} = 0$ or $k = \frac{m^*}{2\hbar}(\alpha_1 + \alpha_2)$, respectively. The energy difference between this lowest-energy transition and the first transition between spin-degenerate bands, which occurs at $k = 0$ with an energy of $E_2(0) - E_1(0)$, is $\Delta E = \frac{m^*}{4\hbar^2}(\alpha_1 + \alpha_2)^2$. Finally, the sum α of the Rashba parameters of the valence and conduction band is given by

$$\alpha = |\alpha_1 + \alpha_2| = 2\hbar\sqrt{\frac{\Delta E}{m^*}}.$$

With the experimental ΔE and a value $m^* = 0.3\ m_0$ in agreement with calculations (21, 22), we estimate $\alpha \approx 3$ eV Å. As discussed in the main manuscript, calculations show a larger Rashba splitting in the conduction than in the valence band. In the limiting case that Rashba splitting in the valence band is neglected, α gives an estimate of the Rashba parameter in the conduction band.

1. Liu Y, et al. (2015) Two-Inch-Sized Perovskite $CH_3NH_3PbX_3$ (X= Cl, Br, I) Crystals: Growth and Characterization. *Adv. Mater.* 27(35):5176.
2. Shrestha S, et al. (2018) Assessing Temperature Dependence of Drift Mobility in Methylammonium Lead Iodide Perovskite Single Crystals. *J. Phys. Chem. C* 122(11):5935.
3. Eames C, et al. (2015) Ionic transport in hybrid lead iodide perovskite solar cells. *Nat. Commun.* 6:7497.
4. Li C, et al. (2016) Iodine migration and its effect on hysteresis in perovskite solar cells. *Adv. Mater.* 28(12):2446.
5. Yi HT, Wu X, Zhu X, Podzorov V (2016) Intrinsic Charge Transport across Phase Transitions in Hybrid Organo-Inorganic Perovskites. *Adv. Mater.* 28(30):6509.
6. Varshni Y (1967) Band-to-band radiative recombination in groups IV, VI, and III-V semiconductors (I). *Phys. Status Solidi (b)* 19(2):459–514.
7. Elliott RJ (1957) Intensity of optical absorption by excitons. *Phys. Rev.* 108(6):1384.
8. Feneberg M, et al. (2013) Anisotropic absorption and emission of bulk (1 1¯ 00) AlN. *Phys. Rev. B* 87(23):235209.
9. Niesner D, et al. (2017) Temperature-dependent optical spectra of single-crystal $CH_3NH_3PbBr_3$ cleaved in ultrahigh vacuum. *Phys. Rev. B* 95(12):075207.
10. Yang Z, et al. (2017) Unraveling the Exciton Binding Energy and the Dielectric Constant in Single-Crystal Methylammonium Lead Triiodide Perovskite. *J. Phys. Chem. Lett.* 8(8):1851.
11. Wehrenfennig C, Liu M, Snaith HJ, Johnston MB, Herz LM (2014) Homogeneous Emission Line Broadening in the Organo Lead Halide Perovskite $CH_3NH_3PbI_{3-x}Cl_x$. *J. Phys. Chem. Lett.* 5(8):1300–1306.
12. Li B, et al. (2017) Polar rotor scattering as atomic-level origin of low mobility and thermal conductivity of perovskite $CH_3NH_3PbI_3$. *Nat. Commun.* 8:16086.
13. Wu X, et al. (2017) Light-induced picosecond rotational disordering of the inorganic sublattice in hybrid perovskites. *Sci. Adv.* 3(7):e1602388.
14. Milot RL, Eperon GE, Snaith HJ, Johnston MB, Herz LM (2015) Temperature-Dependent Charge-Carrier Dynamics in $CH_3NH_3PbI_3$ Perovskite Thin Films. *Adv. Func. Mater.* 25(39):6218–6227.
15. Dar MI, et al. (2016) Origin of unusual bandgap shift and dual emission in organic-inorganic lead halide perovskites. *Sci. Adv.* 2(10):e1601156.
16. Diab H, et al. (2016) Narrow Linewidth Excitonic Emission in Organic-Inorganic Lead Iodide Perovskite Single Crystals. *J. Phys. Chem. Lett.* 7(24):5093.
17. Wu X, et al. (2015) Trap states in lead iodide perovskites. *J. Am. Chem. Soc.* 137(5):2089–2096.
18. Galkowski K, et al. (2017) Spatially resolved studies of the phases and morphology of methylammonium and formamidinium lead tri-halide perovskites. *Nanoscale* 9:3222.
19. Miyata A, et al. (2015) Direct measurement of the exciton binding energy and effective masses for charge carriers in organic-inorganic tri-halide perovskites. *Nat. Phys.* 11(7):582.
20. Ogawa N, Bahramy MS, Kaneko Y, Tokura Y (2014) Photocontrol of Dirac electrons in a bulk Rashba semiconductor. *Phys. Rev. B* 90(12):125122.
21. Umari P, Mosconi E, De Angelis F (2014) Relativistic GW calculations on $CH_3NH_3PbI_3$ and $CH_3NH_3SnI_3$ perovskites for solar cell applications. *Sci. Rep.* 4:4467.
22. Mosconi E, Umari P, De Angelis F (2016) Electronic and optical properties of MAPbX 3 perovskites (X= I, Br, Cl): a unified DFT and GW theoretical analysis. *Phys. Chem. Chem. Phys.* 18(39):27158.
23. Hutter EM, et al. (2016) Direct-indirect character of the bandgap in methylammonium lead iodide perovskite. *Nat. Mater.* 16:115.
24. Wang T, et al. (2017) Indirect to direct bandgap transition in methylammonium lead halide perovskite. *Energy Environ. Sci.* 10:509.
25. Huang W, et al. (2018) Observation of Unusual Optical Band Structure of $CH_3NH_3PbI_3$ Perovskite Single Crystal. *ACS Photon.* 5(4):1583.
26. Sekimoto T, et al. (2018) Energy level diagram of $HC(NH_2)_2PbI_3$ single crystal evaluated by electrical and optical analyses. *Phys. Chem. Chem. Phys.* 20(3):1373.
27. Wu B, et al. (2016) Discerning the surface and bulk recombination kinetics of organic–inorganic halide perovskite single crystals. *Adv. Energy Mater.* 6(14):1600551.
28. Murali B, et al. (2016) Surface Restructuring of Hybrid Perovskite Crystals. *ACS Energy Lett.* 1:1119.
29. Chen F, et al. (2017) Crystal structure and electron transition underlying photoluminescence of methylammonium lead bromide perovskites. *J. Mater. Chem. C* 5(31):7739.
30. Guo D, et al. (2017) Photoluminescence from radiative surface states and excitons in methylammonium lead bromide perovskites. *J. Phys. Chem. Lett.* 8(17):4258.
31. Lechner V, et al. (2011) Spin and orbital mechanisms of the magnetogyrotropic photogalvanic effects in $GaAs/Al_xGa_{1-x}As$ quantum well structures. *Phys. Rev. B* 83(15):155313.
32. Jusserand B, Richards D, Allan G, Priester C, Etienne B (1995) Spin orientation at semiconductor heterointerfaces. *Physical Review B* 51(7):4707.
33. Weber W, et al. (2005) Demonstration of Rashba spin splitting in GaN-based heterostructures. *Appl. Phys. Lett.* 87(26):262106.
34. Schmult S, et al. (2006) Large bychkov-rashba spin-orbit coupling in high-mobility $gan/al_xga_{1-x}n$ heterostructures. *Phys. Rev. B* 74(3):033302.
35. Thillosen N, Schäpers T, Kaluza N, Hardtdegen H, Guzenko VA (2006) Weak antilocalization in a polarization-doped al x ga 1- x n/ ga n heterostructure with single subband occupation. *Applied physics letters* 88(2):022111.
36. Kurdak C, Biyikli N, Özgür Ü, Morkoç H, Litvinov V (2006) Weak antilocalization and zero-field electron spin splitting in al x ga 1- x n/ aln/ gan heterostructures with a polarization-induced two-dimensional electron gas. *Physical Review B* 74(11):113308.
37. Belyaev AE, Raicheva VG, Kurakin AM, Klein N, Vitusevich SA (2008) Investigation of spin-orbit interaction in algan/gan heterostructures with large electron density. *Phys. Rev. B* 77(3):035311.
38. Zhang Q, et al. (2010) Strong circular photogalvanic effect in ZnO epitaxial films. *Appl. Phys. Lett.* 97(4):041907.
39. Lew Yan Voon LC, Willatzen M, Cardona M, Christensen NE (1996) Terms linear in k in the band structure of wurtzite-type semiconductors. *Phys. Rev. B* 53(16):10703–10714.
40. Obraztsov PA, et al. (2018) Ultrafast zero-bias photocurrent and terahertz emission in hybrid perovskites. *Commun. Phys.* 1(1):14.
41. Martin C, et al. (2017) Experimental determination of the bulk rashba parameters in bitebr. *EPL (Europhysics Letters)* 116(5):57003.
42. Niesner D, et al. (2016) Giant Rashba Splitting in $CH_3NH_3PbBr_3$ Organic-Inorganic Perovskite. *Phys. Rev. Lett.* 117:126401.
43. Zhai Y, et al. (2017) Giant rashba splitting in 2d organic-inorganic halide perovskites measured by transient spectroscopies. *Science advances* 3(7):e1700704.

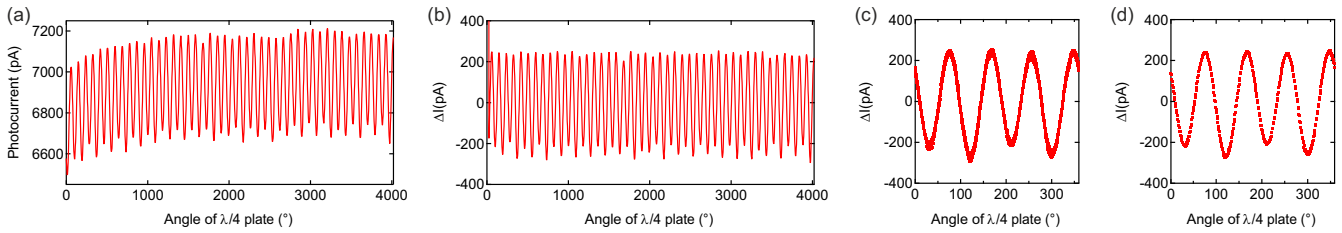

Fig. S1. Analysis of the polarization-dependent photocurrents. From the raw data (a) first a sliding average is subtracted to account for slow fluctuations in laser power (b). The data are then projected onto an interval of 360° (c) and averaged to steps of 1° (d).

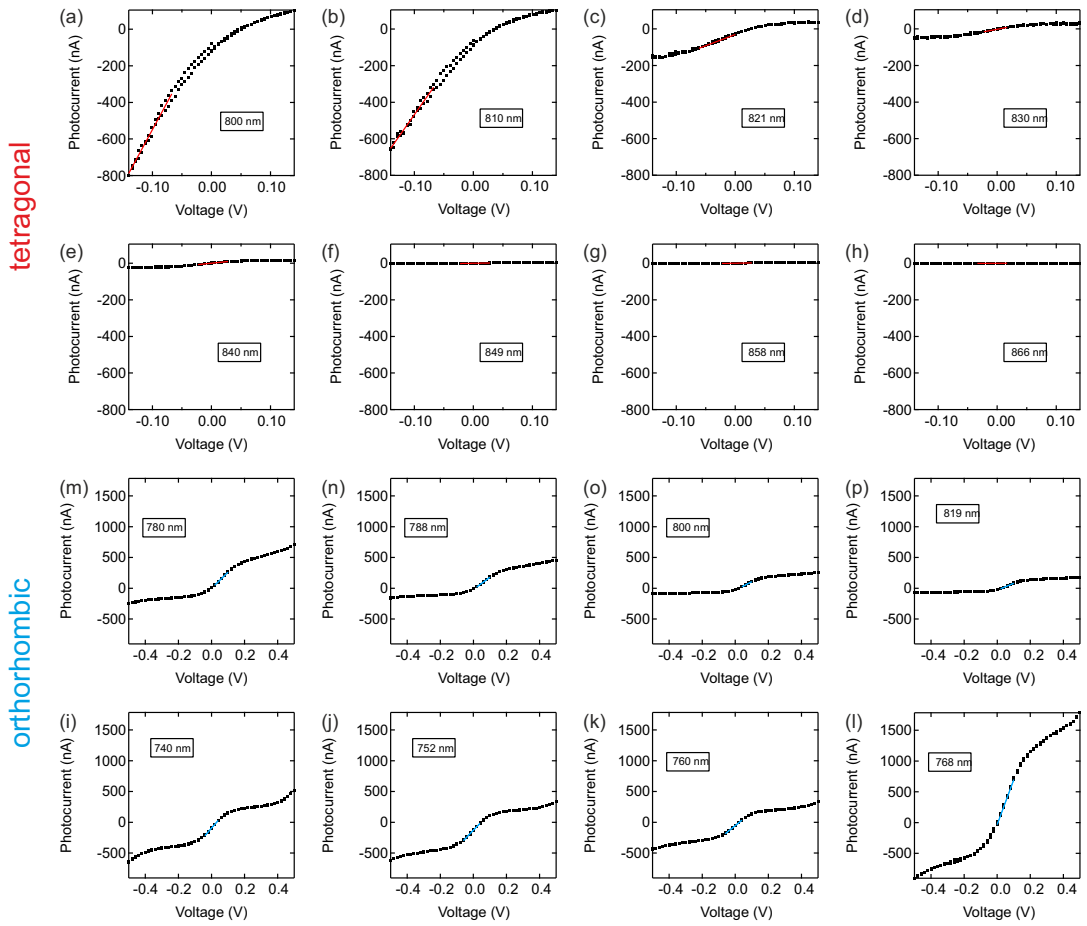

Fig. S2. I(U)-curves under illumination at different laser wavelenghts for the room-temperature tetragonal phase (a - h) and the low-temperature orthorhombic phase (m - l). The maximum slope (red and blue linear fits) is used as a measure of the photoconductivity.

Sample number	1	2	3	4	5	6	7	8
wavelength dependence of C (4 K)	S8						3 (c, d), S8	
wavelength-dependent photoconductivity (4 K)	3 (d)							
wavelength dependence of C (290 K)			3 (a, b), S8	S8				5, S8
wavelength-dependent photoconductivity (290 K)		3 (b)						
ϑ dependence (290 K)			2 (b)	2 (a, b)				
temperature-dependent C					4 (a, b), S8	S8		5, S8
photoluminescence	S4							5, S3

Table S1. List of measurements performed on the samples under investigations. Numbers and letters indicate the figures showing the corresponding data.

Material	E_1	E_2	ΔE	technique	assignment	Ref.
$(CH_3NH_3)PbI_3$	-	-	0.047	MWC, PL (*)	indirect/direct gap	(23)
	1.55	1.61	0.06	T, PL (**)	indirect/direct gap (Rashba)	(24)
	1.48	1.58	0.10	R, PL, PC	different localization in unit cell	(25)
$(HCN(NH_2)_2)PbI_3$	1.40	1.52	0.12	T, R, PC	bulk vs surface	(26)
$(CH_3NH_3)PbBr_3$	2.22	2.30	0.08	PL	bulk vs surface	(27)
	2.25	2.37	0.12	R	bulk vs surface	(27)
	2.22	2.28	0.06	R, PL, TA	bulk vs surface	(28)
	2.22	2.31	0.09	PL, TPPL	-	(9)
	2.22	2.31	0.09	PL	phase coexistence	(29)
	2.14	2.27	0.13	PL	bulk vs surface	(30)
	2.20	2.30	0.10	R, PL	small and large polarons	(30)

Table S2. Reported dual near-bandgap optical transitions for single-crystal lead halide perovskites at room temperature. Transition energies E_1, E_2 as well as their difference ΔE in eV.
Techniques: MWC - microwave conductivity, PL - photoluminescence, T -transmission, R - reflectance, PC - photocurrent spectroscopy, TA - transient absorption, TPPL - two-photon induced photoluminescence.
(*) experiments done on thin films as a function of temperature across several phases.
(**) experiments done on thin films as a function of pressure across several phases.

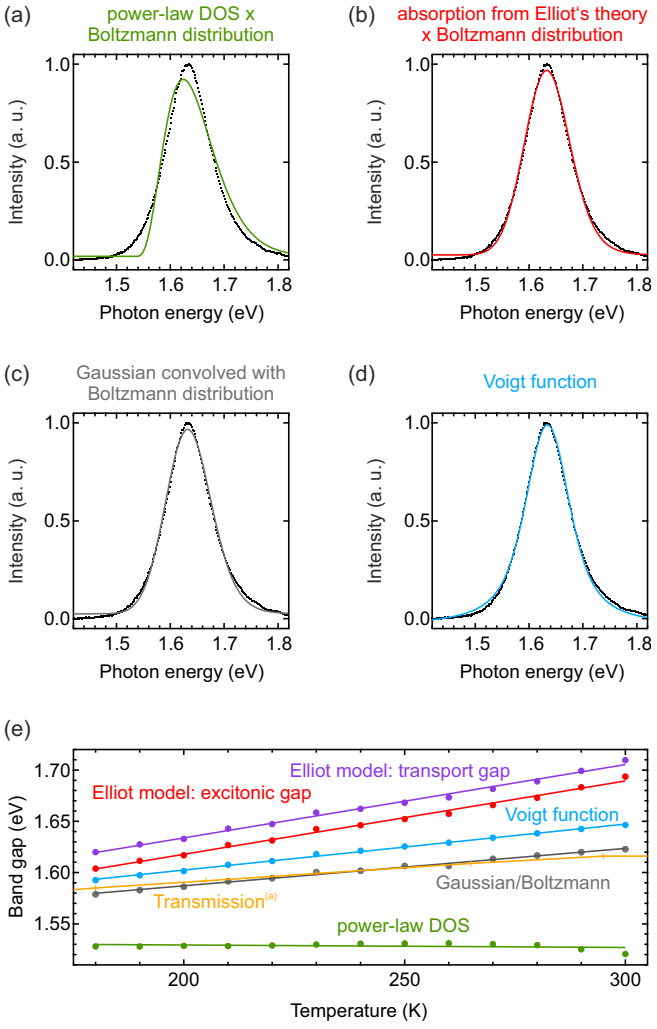

Fig. S3. Photoluminescence spectrum of $(CH_3NH_3)PbI_3$ perovskite single crystal at 270 K under cw illumination, and fits of different model functions to the data (a - d). The extracted values of the optical band gap are summarized in (e). The band gaps measured in transmission experiments on thin films (yellow data points) from [a] Ref. (14) are given for comparison.

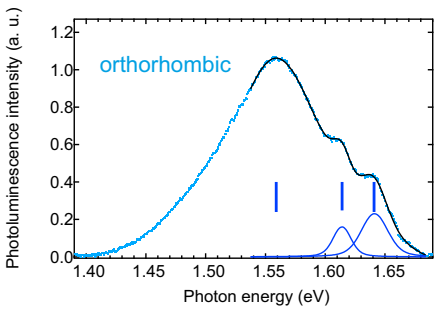

Fig. S4. Photoluminescence spectra of $(CH_3NH_3)PbI_3$ in the low-temperature orthorhombic phase. A fit using three Gaussian peaks is shown as a blue curve. Peak positions are indicated by vertical marks.

Material	Form	C (μA/W)	α_R (eVÅ)
Wurtzite semiconductors			
$GaAs/Al_xGa_{1-x}As$	QW	0.001 (31)	0.007 (32)
$GaN/Al_xGa_{1-x}N$	QW	0.002 (33)	$\leq$ 0.01 (34–37)
ZnO	PC	0.1 (38)	0.004 (39)
Lead halide perovskites			
$(CH_3NH_3)PbI_3$	SC	1	1.6...11*
	PC	$>$ 1000 (40)	
Bulk Rashba systems			
BiTeBr	SC	0.1 (20)	1.7 (41)

Table S3. CPE amplitude C and Rashba parameter α_R of different material systems. SC: single crystal, PC: polycrystalline thin film, QW: quantum well structure.
*** since no experimental data are available for $(CH_3NH_3)PbI_3$, we give the values for the related $(CH_3NH_3)PbBr_3$ (42) and $(C_6H_5C_2H_4NH_3)_2PbI_4$ (43) LHPs.**

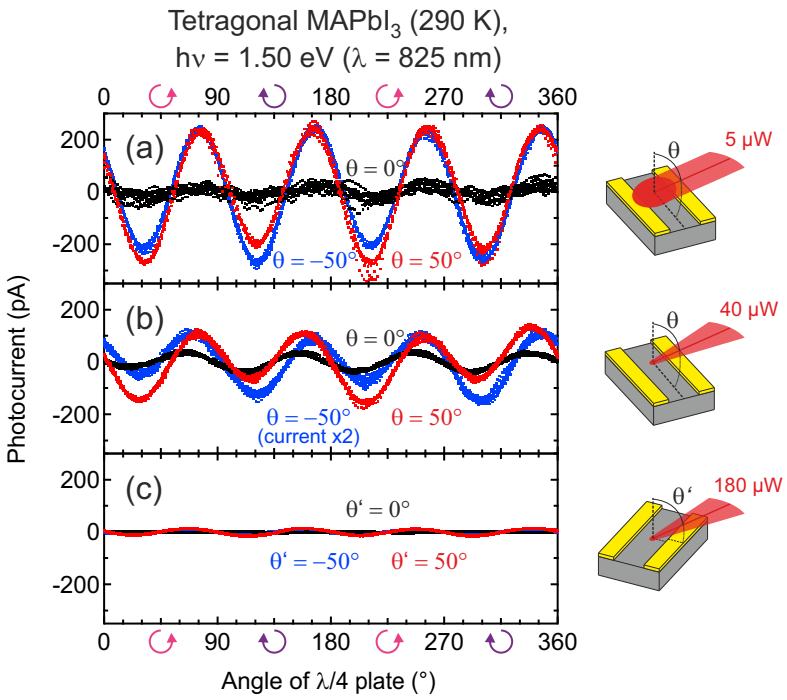

Fig. S5. Light-polarization-dependent changes in the photocurrent. Data are given for a positive (red) and a negative (blue) angle of light incidence, as well as for normal incidence (black), and for the three different experimental geometries depicted to the right: (a) parallel excitation beam, (b) focused laser beam, (c) focused beam, sample rotated by $90°$.

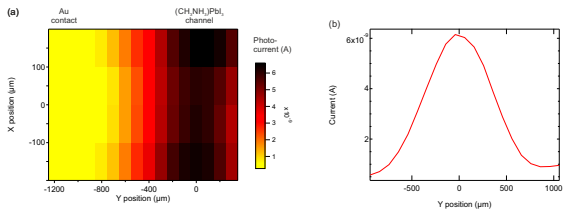

Fig. S6. Spatial variation of the photocurrent as the laser is scanned across the device. (a) gives a two-dimensional representation of the photocurrent as a function of the position of the laser spot. The channel width of the device along the y-direction is 1 mm, the length of the devices along the x-direction $\geq$ 3 mm. The laser spot size was estimated from convolving a Gaussian with the dimensions of the device. A cross-section of the photocurrent is given in (b).

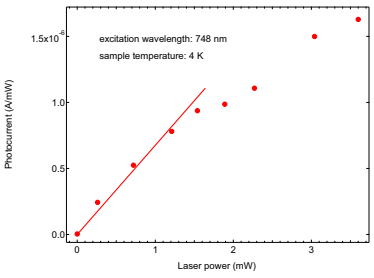

Fig. S7. Intensity-dependence of the measured photocurrents. A linear fit to the data is shown for intensities $<$ 1 mW.

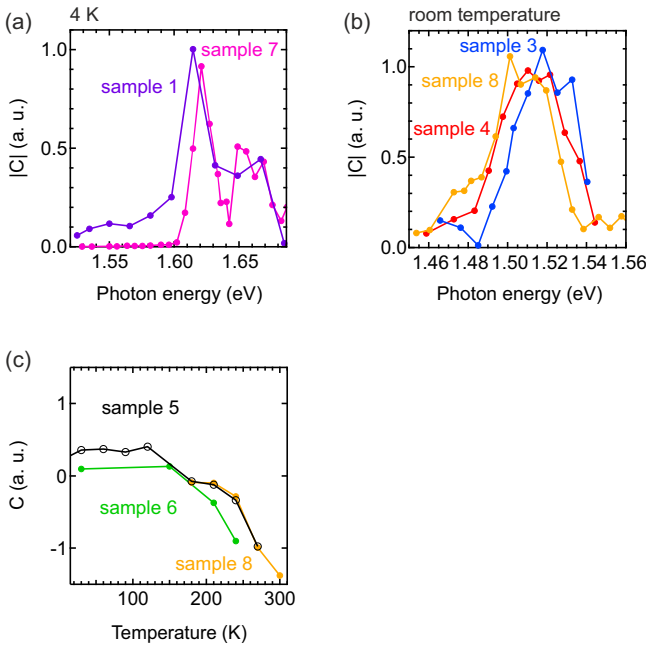

Fig. S8. Amplitude C of the CPE in control measurements on different samples. The numbering of the samples refers to table S1. Amplitudes are normalized for better visibility. (a) and (b) show the photon-energy dependence of $|C|$ in the low-temperature (4 K) orthorhombic and the room-temperature tetragonal phase. To measure the temperature-dependence shown in (c), sample 5 was heated monotonously from 4 K to room temperature, whereas sample 6 was cycled through the phase transition at $\approx$ 160 K (measurements were first taken at 210 K, then at 150 and 30 K, and finally at 240 K). Sample 8 was kept in the room-temperature phase and not cooled below the orthorhombic-tetragonal phase transition temperature. In (c), the excitation photon energy was 1.51 eV for temperatures $>$ 160 K and 1.64 eV for temperatures $<$ 160 K.